

# Ultralow Loading Fe on N-Doped Carbon Nanospheres for Anaerobic Cleavage of C–C Bonds in Biomass Vicinal Diols

Fei-Feng Mao, Yi-An Wang, Yan Zhou,\* Ming-Shuai Sun, Wei Hui,\* and Duan-Jian Tao

Cite This: *ACS Appl. Nano Mater.* 2024, 7, 19386–19396

Read Online

ACCESS |



Metrics &amp; More



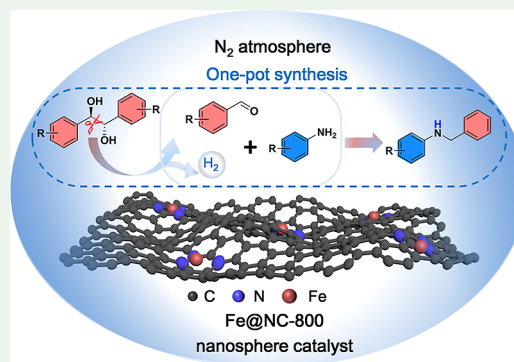
Article Recommendations



Supporting Information

**ABSTRACT:** The efficient and selective conversion of biomass-derived vicinal diols into high-value-added chemicals represents a pivotal area of research that has garnered substantial interest within the scientific community. In this work, three ultralow loading Fe supports on N-doped carbon nanosphere catalysts (Fe@NC-*T*) were successfully prepared using the hard template method with acid etching. The selective conversion of vicinal diols into aldehydes, ketones, and amines over the Fe@NC-800 nanosphere catalyst was achieved through an anaerobic cleavage of C–C bonds and successfully utilized autologous hydrogen resources. The exceptional catalytic activity of the Fe@NC-800 nanosphere catalyst may be credited to the presence of highly dispersed Fe species at the active sites, which has been verified through several characterization techniques, control tests, and density functional theory calculations. In addition, the Fe@NC-800 nanosphere catalyst also demonstrated its wide applicability and excellent reusability under the operating conditions. We believe that this study presents an auspicious scheme for the highly selective conversion of vicinal diols into high value-added carbonyl compounds and amine products.

**KEYWORDS:** nanosphere, anaerobic cleavage, ultralow-loading Fe-based catalysts, biomass vicinal diols, phenoxy oxygen-containing compounds, amines



## 1. INTRODUCTION

The utilization of organic biomass is increasingly recognized as a key approach for sustainable construction practices.<sup>1,2</sup> In particular, there is rising interest in exploring organic biomass as a source of high-value platform chemicals. One method for the utilization of biomass resources involves the depolymerization of lignin to produce vicinal diols, which are a prominent category of biomass-derived products.<sup>3,4</sup> Therefore, heightened attention has been put toward the selective conversion of vicinal diols into high-value chemicals, as it supports the objective of reducing the dependency on fossil fuel energy.

Recently, considerable attempts have been invested in the efficient transformation of biomass-derived vicinal diols.<sup>5–7</sup> A wide array of catalytic systems has been identified and reported for the aerobic oxidative cleavage of vicinal diols.<sup>8–10</sup> For example, Anasta and his co-workers employed a Na–Mn–LMO catalyst to facilitate the cleavage of C–C bonds in vicinal diols, achieving an outstanding 98% yield of benzaldehyde.<sup>11</sup> Gao and co-workers have described the synthesis of an atomic-scale meso-Co–NC–800 catalyst for converting vicinal diols into ketones, esters, or aldehydes through the aerobic oxidative cleavage method.<sup>12</sup> Moreover, Sun et al. have introduced a NaOtBu–O<sub>2</sub> system for converting vicinal diols into carboxylic acids with yields between 95 and 99%.<sup>13</sup> Therefore, this progress implies that the conversion of vicinal diols via the

aerobic oxidative cleavage method mainly produces various oxygen containing compounds, while water is the byproduct.

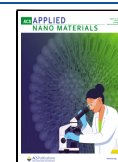
On the other hand, a parallel scheme of direct dehydrogenation of vicinal diols under an inert gas atmosphere is highly attracted and conceived, in which the C–C bonds of vicinal diols can be cleaved along with the generation of H<sub>2</sub>.<sup>14,15</sup> This specific route can be used for synthesizing more valuable products (e.g., imine, amine) by making use of sequent condensation and the H<sub>2</sub> transfer reaction. From this point of view, developing an appropriate catalytic system for the transformation of vicinal diols into targeted aldehydes, ketones, and amines is of great significance. Very recently, atomically dispersed metal catalysts garnered significant interest in heterogeneous catalysis given its maximum atom efficiency. These catalysts, with ultralow metal loading, have shown excellent performance in catalyzing oxidation, hydrogenation, and other important reactions.<sup>16–19</sup> At present, there are numerous reports outlining the use of the hard template

Received: June 8, 2024

Revised: July 24, 2024

Accepted: July 29, 2024

Published: August 5, 2024



method for producing well-dispersed metal catalysts.<sup>20–22</sup> This method primarily involves utilizing the sol–gel technique to create SiO<sub>2</sub> nuclei or directly using colloidal silica nanoparticle dispersion, followed by acid washing to eliminate the SiO<sub>2</sub> nuclei and metal nanoparticles. Usually, this preparation method with a template removal agent has its unique advantages, such as improved pore structure, restoration of surface functional groups, and enhanced thermal stability. After removing the hard template, the material often exhibits an upsurge in specific surface area and pore volume, which is crucial for catalytic applications as it provides more active sites and space.<sup>23</sup>

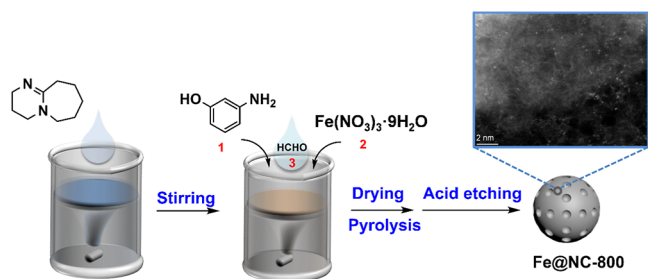
Herein, a series of ultralow loading Fe supported on N-doped carbon nanosphere catalysts (Fe@NC-*T*) were prepared using a hard template method with acid etching. Then, the anaerobic C–C bonds cleavage of vicinal diols and subsequent H<sub>2</sub> transfer tandem reaction over the Fe@NC-*T* nanosphere catalysts were conducted for synthesis of corresponding aldehydes, ketones, and amines, respectively. Furthermore, a range of characterizations, control experiments, and density functional theory (DFT) analyses were performed to reveal the catalysis of Fe@NC-*T* nanosphere catalysts. Additionally, the adaptability and recyclability of the Fe@NC-800 nanosphere catalyst were finally examined.

## 2. EXPERIMENTAL SECTION

**2.1. Materials.** Meso-1,2-diphenyl-1,2-ethanediol (99 wt %), tetraphenylethylene (95 wt %), (2*R*)-1,1,2-triphenylethylene glycol (98 wt %), (*R,R*)-(+)-hydrobenzoin (99 wt %), and (±)-hydrobenzoin (98 wt %) were supplied by Shanghai Aladdin Co. Ltd. (*S*)-1,1-diphenyl-1,2-propanediol (99 wt %) was purchased from Daicel chiral technologies Co. Ltd. Details for the synthesis of non-commercially available disubstituted vicinal diols were shown in the Supporting Information. 3-aminophenol (98 wt %), ferric nitrate nonahydrate [Fe(NO<sub>3</sub>)<sub>3</sub>·9H<sub>2</sub>O, 98.5%], 1,5-diazabicyclo(5,4,0)-undec-5-ene (DBU, 98 wt %), and formaldehyde (37 wt %) were provided by the Shanghai Macklin Co., Ltd. Fumed silica (30 wt %) was obtained from Sigma-Aldrich Co., Ltd. Furthermore, no further purification was conducted on any of the chemicals before their use.

**2.2. Preparation Process for the Fe@NC-*T* Nanosphere Catalysts.** Scheme 1 shows a brief preparation process of the Fe@

**Scheme 1. Preparation of the Fe@NC-800 Nanosphere Catalyst in This Work**



NC-800 nanosphere catalysts. First, mixed solution was created by combining 0.5 g of DBU and 5 g of fumed silica in 20 mL of deionized water. Subsequently, 0.5 g of 3-aminophenol followed by 0.1 g of Fe(NO<sub>3</sub>)<sub>3</sub>·9H<sub>2</sub>O were sequentially added into the aforementioned solution with continuous stirring maintained for 0.5 h. Then, 1 mL of formaldehyde was gradually dripped into the mixture and immediately polymerized with the aminophenol to form a yellow suspension. At a maintained temperature of 50 °C, the solution was agitated for 24 h. During this process, the iron was encapsulated, and the color of the solution deepened to a brownish-

yellow hue. After centrifugation to collect the brownish-yellow precursor, the mixture was washed a total of five times using deionized water. Thereafter, the precursor was taken to a vacuum oven, where it was dried at 80 °C over 8 h. Next, the dry precursor was subsequently placed in a tubular furnace and exposed to a nitrogen atmosphere at a flow rate of 30 mL/min for 30 min. The tubular furnace temperature was progressively elevated from 30 to 800 °C at a ramp of 5 °C/min and maintained at the peak temperature for 2 h. The obtained powder was named as Fe@NC-800/SiO<sub>2</sub>. Furthermore, the Fe@NC-800/SiO<sub>2</sub> catalyst was processed by immersing it in a 10 wt % hydrofluoric acid solution to remove the silica and then washed with deionized water until neutral. Thereafter, the acquired powder was subjected to drying at 60 °C within a vacuum oven for 24 h, after which it was named as Fe@NC-800. For comparison, Fe@NC-600 and Fe@NC-1000 nanosphere catalysts were synthesized with the same procedure of the Fe@NC-800 with the annealing temperatures being altered to 600 and 1000 °C, respectively. Moreover, Fe–N–C-800, NC-800, and Fe–C-800 catalysts were synthesized without silica, Fe(NO<sub>3</sub>)<sub>3</sub>·9H<sub>2</sub>O and DBU, respectively.

**2.3. Catalyst Characterization.** The nitrogen adsorption–desorption isotherms of the as-prepared catalysts were measured with a Micromeritics TriStar II 3020 analyzer. Surface morphological structures of the samples were observed by scanning electron microscopy (SEM) on a HITACHI SU8020 instrument. Detailed information on sample morphologies were analyzed by transmission electron microscope (TEM) and high-resolution electron microscope on a JEOL JEM-2100 instrument. The element distribution of the as-prepared catalysts was analyzed by aberration-corrected high-angle annular dark-field scanning transmission electron microscopy (HAADF-STEM) on a JEM-ARM300F device. XRD measurements were taken on a Rigaku RINT-2200 X-ray diffractometer, utilizing a Cu K $\alpha$  radiation source. Raman spectroscopy data were obtained on a Jobin Yvon LabRAM HR spectrometer. NMR analysis was conducted on a Bruker AVANCE 400 spectrometer with frequencies of 400 MHz for <sup>1</sup>H and 101 MHz for <sup>13</sup>C. And the NMR spectra of noncommercially available disubstituted vicinal diols are provided in Supporting Information. CO<sub>2</sub> temperature-programmed desorption (CO<sub>2</sub>-TPD) experiments were performed by utilizing a Micromeritics Autochem II 2920 chemisorption analyzer. Surface valence states of the as-prepared catalysts were examined by X-ray photoelectron spectroscopy (XPS) using an AXIS Ultra instrument from Kratos Analytical. Moreover, the detailed information on CO<sub>2</sub>-TPD and XPS analysis was supplied in Supporting Information (S1.1 and S1.2). The H<sub>2</sub> and N<sub>2</sub> signals were detected by a FULI GC-960 with a thermal conductivity detector. The Fe content of as-prepared catalysts was measured by inductively coupled plasma optical emission spectrometry (ICP-OES) on an Agilent 720 instrument. The thermal stability of the samples was measured by thermogravimetric-differential thermal analyzer (TG 6300, SEIKO).

**2.4. Catalytic Activity Test.** For the synthesis of *N*-benzylaniline, a standard procedure was followed. Meso-hydrobenzoin (0.35 mmol), aniline (0.25 mmol), and a catalyst (30 mg) were accurately weighed and placed in a 25 mL stainless steel autoclave. Toluene (5 mL) was used as the solvent for the reaction. The air within the reactor was repeatedly purged with pure N<sub>2</sub>, followed by maintaining a N<sub>2</sub> pressure of 0.4 MPa. The reaction took place at a steady temperature of 160 °C for a duration of 24 h, agitated by a magnetic stirrer operating at a speed of 600 rpm. Once the reaction mixture had cooled to the temperature of the room temperature, it was filtered. The liquid phase products were then quantitatively analyzed using a Thermo Trace 1310 gas chromatograph (GC) equipped with a flame ionization detector. The GC featured a TG-SHT capillary column with specifications, including a length of 30 m, an internal diameter of 0.25 mm, and a film thickness of 0.25  $\mu$ m. The specific test procedure information is available in the Supporting Information (S1.3). The products were qualitatively analyzed by GC–MS using a Thermo Trace 1300 GC-ISQ system. In addition, for the recovery and reuse of the catalyst, the Fe@NC-800 nanosphere catalyst was isolated from the reaction mixture by using centrifugation once the reaction was

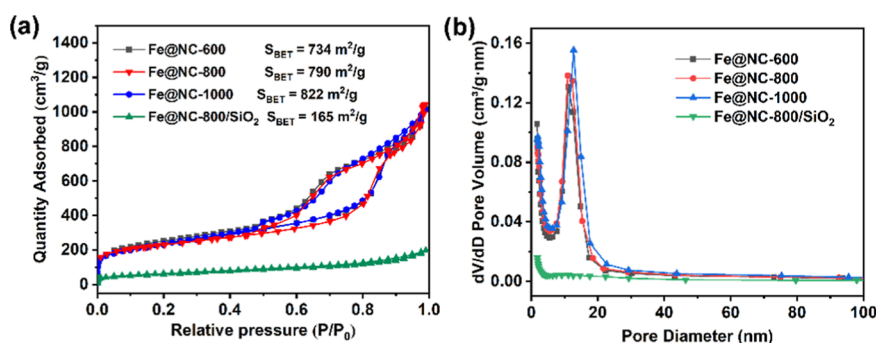


**Figure 1.** (a) The N<sub>2</sub> adsorption–desorption isotherms of Fe@NC-*T* (*T* = 600, 800, 1000 °C) and Fe@NC-800/SiO<sub>2</sub>, (b) pore size distribution curves.

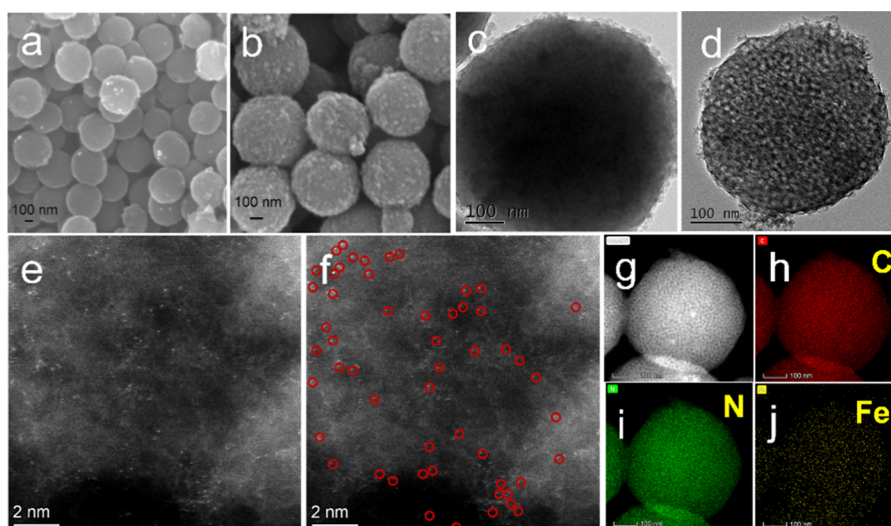


**Figure 2.** SEM images of (a) Fe@NC-800, (b) Fe@NC-800/SiO<sub>2</sub>, TEM images of (c) Fe@NC-800/SiO<sub>2</sub>, (d) Fe@NC-800, (e) HAADF-STEM image, and (f) version highlighted by red circles. (g–j) Corresponding elemental mapping for Fe@NC-800 (red stands for carbon, yellow for iron, and green for nitrogen).

concluded. Subsequently, they underwent a series of six ethanol washes ( $6 \times 10$  mL) to remove any residual impurities. After the washing process, the catalyst was subjected to drying at 80 °C in a vacuum oven for a duration of 6 h to eliminate any remaining moisture or solvent traces and subsequently utilized again in the next catalytic experiment.

### 3. RESULTS AND DISCUSSION

**3.1. Characterization of the Fe@NC-*T* Nanosphere Catalysts.** The nitrogen adsorption-desorption isotherm tests were conducted at  $-196$  °C to determine the pore structure properties and pore size distribution of the as-prepared catalysts. As depicted in Figure 1a, the Fe@NC-*T* (*T* = 600, 800, 1000 °C) nanosphere catalysts exhibit the typical features of type IV isotherms as classified by the IUPAC, which means that their porous structures are mainly mesoporous. Additionally, the presence of H<sub>3</sub> type hysteresis loops within the adsorption–desorption isotherms further confirms the mesoporous nature of the Fe@NC-*T* nanosphere catalysts.<sup>24–26</sup> These observations are supported by the pore size distribution curves of the Fe@NC-*T* nanosphere catalysts (Figure 1b). The distribution curves reveal that the pore-size centers of three catalysts are between 10 and 20 nm, which were calculated according to the Barret–Joyner–Halenda model. This underscores the reproducible nature of the mesoporous structure across different carbonization temperature. In contrast, the

Fe@NC-800/SiO<sub>2</sub> catalyst displays a type III isotherm, suggesting a different pore structure.<sup>27,28</sup> This disparity indicates a distinct variation in the structure of the pores, which is probably impacted by limitations imposed by the SiO<sub>2</sub> template. Besides, the structural properties of the catalysts were further clarified through the calculation of their specific surface areas by the BET method. Specifically, the specific surface areas of the Fe@NC-*T* nanosphere catalysts are 734, 790 and 822 m<sup>2</sup>/g, respectively. Interestingly, the gradual rise in surface area as the temperature of calcination increases indicates an increase in porosity and potentially stronger catalytic activity at elevated temperatures. However, the Fe@NC-800/SiO<sub>2</sub> catalyst shows a markedly decreased specific surface area, measured at a mere 165 m<sup>2</sup>/g. This substantial reduction highlights the significant impact of the SiO<sub>2</sub> template removal on the specific surface area characteristics of the Fe@NC-*T* nanosphere catalyst. Therefore, the comparison starkly emphasizes the critical role that synthetic conditions and compositional variations play in tailoring the physicochemical properties of catalytic materials for the optimized performance in chemical reactions.

The synthesized catalysts were characterized for their morphological and structural features using SEM and TEM instrument. As depicted in Figure 2a,b, the SEM images of the Fe@NC-800 and Fe@NC-800/SiO<sub>2</sub> catalysts reveal a distinct



spherical shape with uniform dimensions. A comparative analysis of the TEM images for Fe@NC-800 (Figure 2c) and Fe@NC-800/SiO<sub>2</sub> catalysts (Figure 2d) indicates the presence of clear surface furrows on Fe@NC-800, which are believed to be a consequence of the acid treatment during synthesis.

Notably, the absence of visible metal nanoparticles in Figure 2d implies that the Fe species are extensively dispersed throughout the catalyst. This dispersion is indicative of a potentially active catalytic phase, where the Fe species are likely integrated at the molecular level, suggesting a high degree of atomic dispersion. Furthermore, this observation was further confirmed through HAADF-STEM (see Figure 2e,f), where numerous bright dots highlighted with red circles are homogeneous distributed across the catalyst, revealing the existence of isolated Fe species.<sup>29,30</sup> These bright dots, with sizes of roughly 0.2 nm, reconfirm the presence of dispersed Fe species. Additionally, the elemental mappings of the Fe@NC-800 nanosphere catalyst exhibit its compositional details (see Figure 2g–j). The results reveal a uniform distribution of carbon (C), nitrogen (N), and iron (Fe) elements within the Fe@NC-800 nanosphere catalyst. Additionally, the Fe loading in the Fe@NC-800 nanosphere catalyst was determined to be 0.19 wt % through ICP-OES analysis, as detailed in Table 1.

**Table 1. Textural Properties of Different Catalysts**

samples	pore volume (cm <sup>3</sup> /g)	pore size (nm)	Fe content <sup>a</sup> (wt %)
Fe@NC-600	1.37	9.67	0.13
Fe@NC-800	1.56	9.88	0.19
Fe@NC-1000	1.81	10.33	0.29
Fe@NC-800/SiO <sub>2</sub>	0.22	13.53	6.54
Fe–N–C-800	0.31	5.30	12.89
Fe–C-800	0.30	5.07	14.25
NC-800	0.0019	4.99	

<sup>a</sup>Measured by ICP-OES.

Besides, the morphology and structure of NC-800, Fe@NC-600 and Fe@NC-1000 nanosphere catalysts closely resembled those of the Fe@NC-800 nanosphere catalyst (Figure S1). However, the Fe–N–C-800 catalyst, prepared without the use of the SiO<sub>2</sub> template, consists of agglomerated nanoparticles loaded on support layers (see Figure S2).

The XRD patterns of the as-prepared catalysts were analyzed to elucidate their phase structures, as displayed in Figure 3a. Apparently, the XRD patterns of Fe@NC-*T* nanosphere catalysts exhibit two broad peaks at 23 and 43°, aligning with the diffraction profiles for amorphous carbon and the

(100) planes of carbon with low degree of graphitization, respectively.<sup>31,32</sup> Additionally, the XRD pattern of the Fe@NC-800/SiO<sub>2</sub> catalyst exhibits a diffraction peak at 22°, assignable to the (111) facet of silica.<sup>33,34</sup> Importantly, none of the discernible diffraction peaks associated with Fe species suggest either low Fe loading or uniform distribution of Fe within the catalysts, suggesting either low Fe loading or a uniform distribution of Fe species. These findings are consistent with results obtained from ICP and EDS mapping. Moreover, Raman spectra were employed to assess the defects in these catalysts. The two characteristic peaks at ~1350 and ~1580 cm<sup>-1</sup> are represented as D band and G bands, respectively (see Figure 3b). The intensity ratio of I<sub>D</sub>/I<sub>G</sub> is commonly utilized to quantify the degree of defects in carbon materials.<sup>35,36</sup> Notably, the I<sub>D</sub>/I<sub>G</sub> ratios for Fe@NC-*T* showed a gradual decline from 1.20 to 1.10, suggesting an increase in the degree of defects as the calcination temperature increased.

The various element states on the surfaces of the Fe@NC-*T* nanosphere catalysts were examined by using XPS. The results are plotted in Figures 4 and S3. All energy scales of XPS spectra were calibrated by comparing the C–C peaks of carbon (located at 284.8 eV). Figure S3 shows the survey XPS spectra and C 1s spectra of Fe@NC-600, Fe@NC-800, and Fe@NC-1000 catalysts. In the C 1s spectra, the four deconvoluted peaks are observed at 284.8, 285.51, 288.3, and 290.8 eV. These peaks are attributed to C=C, C–N/C–O, C=N/C=O and O–C=O groups, respectively.<sup>37,38</sup> The result demonstrates that nitrogen was successfully doped into the carbon lattice of the synthesized catalyst. Moreover, the N 1s spectra (see Figure 4a) for Fe@NC-*T* were deconvoluted into four distinct peaks, each corresponding to different bonding forms of nitrogen within the catalysts. Specifically, the peak located at 398.4 eV, which can be attributed to pyridinic N. This type of N is pivotal for enhancing electron density at adjacent carbon sites, which is beneficial for catalytic processes such as oxygen reduction reactions. The peaks observed at 399.4 and 400.8, 403.0 eV, which are associated with Fe–N<sub>x</sub>, graphitic-N, and oxidized-N, respectively.<sup>39–41</sup> The various N contents obtained from semiquantitative analysis are summarized in Table S1. The analysis of the results points to higher pyridinic-N and Fe–N content in the Fe@NC-800 than in the Fe@NC-600 and Fe@NC-1000 nanosphere catalysts. Pyridinic-N is acknowledged for its contribution to the establishment of highly active sites (e.g., Fe–N–C), which are determinant for catalytic proficiency. Moreover, it is well-known that pyridinic-N has a high affinity for Fe atoms. Thus, the high pyridinic-N content in the Fe@NC-800 nanosphere catalyst offers abundant sites to anchor isolated Fe atoms.<sup>42,43</sup>

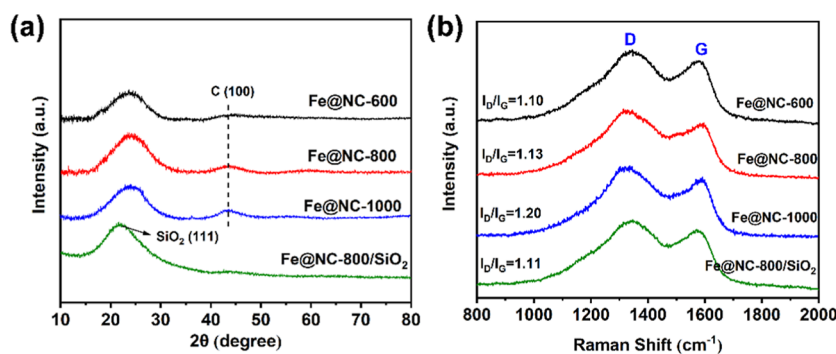


**Figure 3.** (a) XRD patterns and (b) Raman spectra of the Fe@NC-*T* (*T* = 600, 800, and 1000 °C) and Fe@NC-800/SiO<sub>2</sub>.

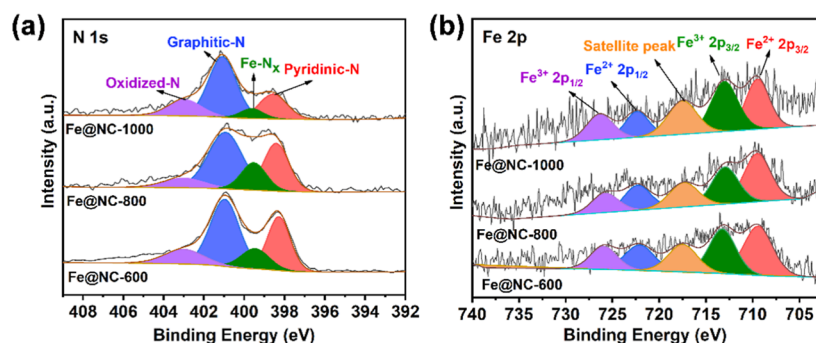


Figure 4. XPS spectra of (a) N 1s, (b) Fe 2p for the Fe@NC-*T* (*T* = 600, 800, and 1000 °C).

Notably, the Fe 2p spectrum further supports the presence of Fe species in the catalysts. These spectra contain five deconvoluted peaks that can be attributed to two types of Fe (II and III) species (see Figure 4b). In detail, the peaks observed at 709.5 and 722.4 eV are ascribed to Fe (III) species, and similarly, the peaks at 712.9 and 725.8 eV are corresponding to Fe (II) species.<sup>44,45</sup> Additionally, the deconvoluted peak located at 717.3 eV is identified as the satellite peak. Overall, the results reconfirm that the catalysts contain ultralow levels of Fe, which is present in the form of multiple valence species.

It is well established that nitrogen doping in carbon materials could lead to charge redistribution, resulting in the formation of electron-rich regions. Furthermore, high-temperature treatment is likely to enhance the formation of surface-active sites, such as pyridine and pyrrole nitrogen.<sup>46,47</sup> The CO<sub>2</sub>-TPD technique was employed to examine the basicity and strength of the Fe@NC-*T* nanosphere catalysts. In general, this methodology provides insights into the basic surface characteristics of catalysts by associating the temperature range and cumulative area of the CO<sub>2</sub> desorption peaks with the strength and abundance of basic sites. Specifically, Figure 5

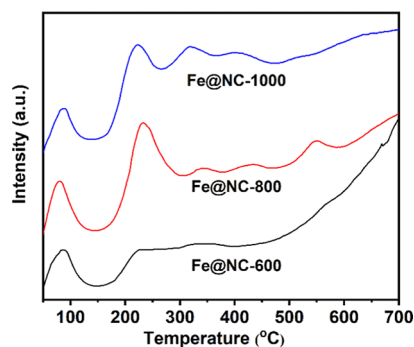


Figure 5. CO<sub>2</sub>-TPD curves for Fe@NC-*T* (*T* = 600, 800, and 1000 °C) in this work.

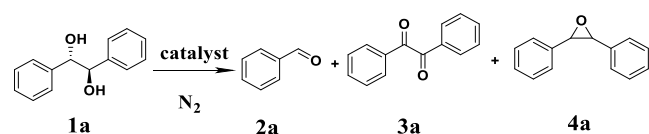
exhibits the CO<sub>2</sub>-TPD profiles of the Fe@NC-*T* nanosphere catalysts, clearly delineating the shifts in peak position and strength with changes in the treatment temperature. The identification of CO<sub>2</sub> desorption peaks across the temperature ranges of 80–150, 200–400, and 600–800 °C are indicative of weak, moderate, and strong basic sites, respectively.<sup>48,49</sup> Besides, the basicity properties of the as-prepared catalyst were calculated based on the CO<sub>2</sub>-TPD data, as listed in Table S2. The Fe@NC-800 nanosphere catalyst exhibits a significant predominance of medium and strong basic sites. This

enhanced basicity suggests a potential for more robust catalytic activity in reactions where strong base sites are advantageous. On the contrary, the Fe@NC-600 and Fe@NC-1000 nanosphere catalysts predominantly feature weak and moderate basic sites. Furthermore, the Fe@NC-800 catalyst stands out with the highest concentration of pyridine nitrogen and Fe-N<sub>x</sub> active sites among these three catalysts. This enrichment of active sites is likely the key factor contributing to the superior basicity of the Fe@NC-800 catalyst, providing a plausible explanation for its enhanced performance in basic site density. Therefore, differences in basic site composition among the catalyst series reveal the impact of thermal treatment on catalyst basicity and suggest potential strategies to improve the performance of catalytic.

### 3.2. Screening of the Fe@NC-*T* Nanosphere Catalysts.

Initially, the catalytic capabilities of various catalysts were evaluated using the cleavage of mesohydrobenzoin (Table 21a) to generate benzaldehyde [Table 2(2a)] as the designated test reaction (Table 2). Obviously, the results of the blank experiment showed that no product was detected in this reaction without any catalyst (Table 2, entry 1). The as-prepared catalysts were further tested in the cleavage of meso-

Table 2. Cleavage of Meso-hydrobenzoin over Various Catalysts<sup>a</sup>



entry	samples	conv 1a (%)	product yield (%) <sup>b</sup>			TOF <sup>d</sup>
			2a	3a	4a	
1			trace	trace	trace	
2	Fe@NC-600	>99	16	4	80	0.14
3	Fe@NC-800	>99	98	trace	2	61.4
4	Fe@NC-1000	91	55	21	15	20.1
5	Fe@NC-800/SiO <sub>2</sub>	26	24	2	trace	0.11
6	NC-800	6	6	trace	trace	
7	Fe-C-800	28	24	4	trace	0.03
8	Fe-N-C-800	21	18	2	<1	0.06
9 <sup>c</sup>	Fe@NC-800	18	16	2	<1	

<sup>a</sup>Reaction conditions: 1a (0.25 mmol), toluene (5 mL), catalyst (0.27 mol %), 110 °C, 6 h, 0.4 MPa N<sub>2</sub>. <sup>b</sup>The outcomes were obtained through GC test with the utilization of an internal standard method and the product was subsequently verified by GC-MS. <sup>c</sup>KSCN (0.25 g) was used. <sup>d</sup>Turnover frequency (TOF) = [mol (product)]/[mol (catalyst) ⊆ time].

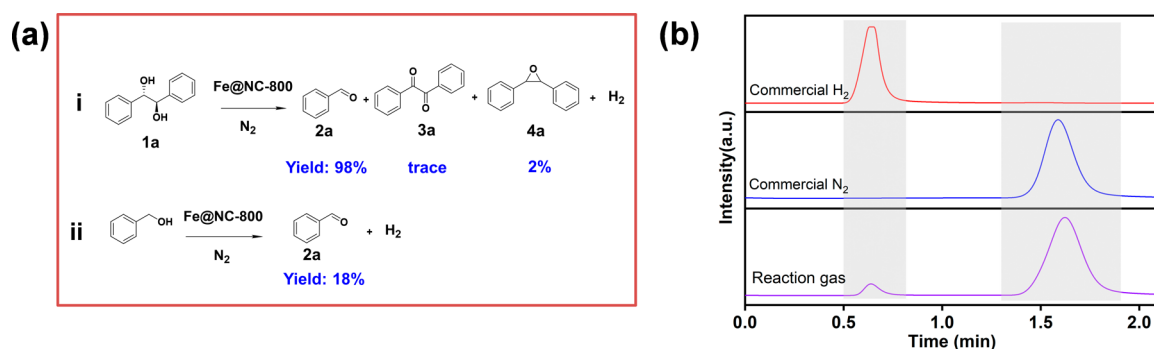


Figure 6. (a) Control experiments. (b) GC spectra of commercial H<sub>2</sub>, commercial N<sub>2</sub>, and the reaction gas.

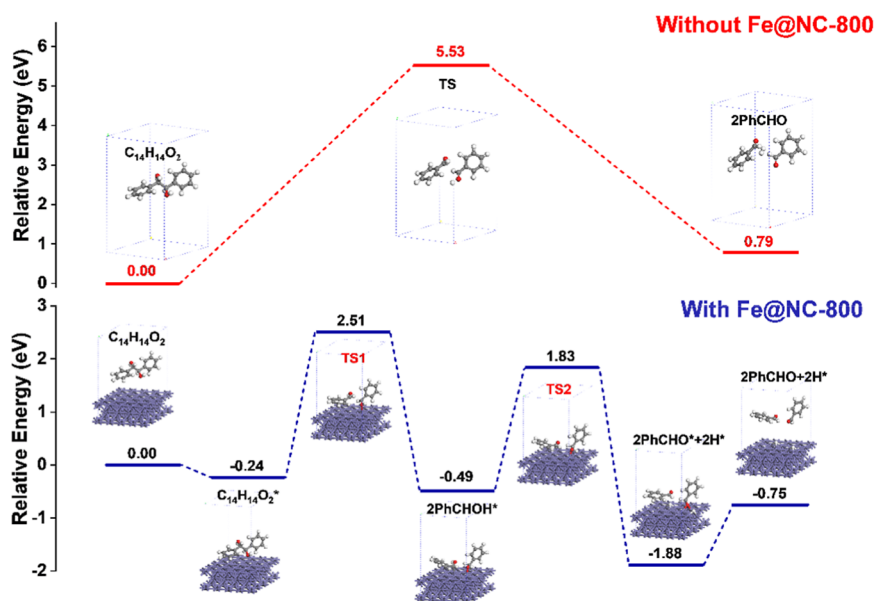


Figure 7. Relative energy profiles of meso-hydrobenzoin cleavage on the Fe@NC-800 surface (route in blue) and its direct breaking of C–C bonds without catalysis (route in red).

hydrobenzoin with the optimization of reaction conditions (Tables 2 and S3). In this work, the optimal parameters for the reaction were determined to be as follows: 0.27 mol % of Fe@NC-800 nanosphere catalyst, nitrogen pressure of 0.4 MPa, temperature of 110 °C, and reaction time of 6 h. The Fe@NC-800 nanosphere catalyst exhibited superior catalytic performance, and the yield of the target product [Table 2(2a)] reached 98%. Moreover, the analysis of the catalytic ability of three ultralow loading Fe@NC-*T* nanosphere catalysts showed that the calcination temperature significantly influences their catalytic performance (Table 2, entries 2–4). Moreover, it was also established that basic sites are indispensable in the dehydrogenation of alcohols.<sup>50,51</sup> Combining this with our prior characterization results, the variations in catalytic activity observed among the aforementioned catalysts could be linked to their specific surface area, active sites, and the quantity of basic sites. When Fe@NC-800/SiO<sub>2</sub> catalyst was carried out in the same reaction, the yield of benzaldehyde was only 24% (Table 2, entry 5), thereby highlighting the significance of the mesoporous structure.

To investigate the active components of the Fe@NC-*T* nanosphere, catalysts were made using the same preparation technique as for Fe@NC-800, but without the inclusion of metal or nitrogen resources, respectively. As a result, Fe–C-800 and NC-800 catalysts exhibited relatively poor catalytic

performance, achieving the target product with 24 and 6% yields, respectively (Table 2, entries 6–7). Additionally, the Fe–N–C-800 catalyst, prepared without SiO<sub>2</sub> template, afforded benzaldehyde with 18% yield (Table 2, entry 8). These findings affirm that the Fe species retained after acid treatment of Fe@NC-800 are crucial for its catalytic activity. Based on previous TEM and experimental results, the isolated Fe species are considered to be the primary active sites in the cleavage of meso-hydrobenzoin reaction. Commonly, KSCN is used to deactivate the active site of the metal center by serving as a binding molecule. To further elucidate the viewpoint, poisoning experiment was carried out with KSCN. As expected, a noticeable reduction in the yield of benzaldehyde was observed (Table 2, entry 9). This confirms the highly dispersed iron species, consistent with the TEM results, and highlights the significant role of isolated Fe species in the reaction of meso-hydrobenzoin cleavage. Furthermore, the turnover frequency (TOF) values of the as-prepared catalysts and other reported catalysts were calculated, as detailed in Tables 2 and S4. The findings revealed that the Fe@NC-800 catalyst demonstrated remarkable effectiveness in the cleavage of meso-hydrobenzoin. Overall, the Fe@NC-800 nanosphere catalyst exhibits exceptional performance and selectivity in facilitating the conversion of biomass-derived substances to benzaldehyde.

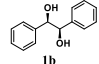
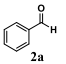
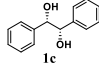
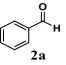
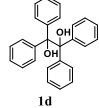
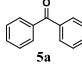
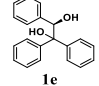
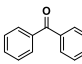
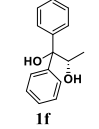
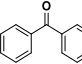
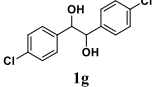
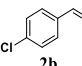
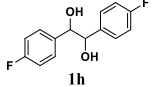
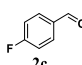
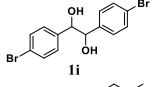
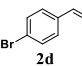
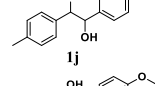
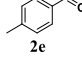
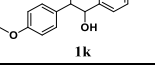
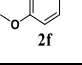
**3.3. Tandem Reaction Pathway Studies.** Based on the results of previous experiments, trace amounts of benzyl product (Table 2, 3a) were detected by GC–MS and GC, which mean that the dehydrogenation of biomass-derived vicinal diols has occurred in the Fe@NC-800 nanosphere catalytic system (Figure 6a, Reaction i). To further validate the accuracy and reliability of this conclusion, the reaction for the cleavage of meso-hydrobenzoin was performed with an Fe@NC-800 nanosphere catalyst under N<sub>2</sub> atmosphere. At the end of the reaction, residual gases were collected from the reactor and analyzed by GC, as depicted in Figure 6b. The presence of H<sub>2</sub> in the residual gases was confirmed by the detection of H<sub>2</sub> signals, which is fully consistent with our predictions. Furthermore, to corroborate this process from another perspective, a simplified model experiment was designed and conducted (see Figure 6a, Reaction ii). In this experiment, benzyl alcohol and Fe@NC-800 nanosphere catalyst were added to a N<sub>2</sub>-filled stainless steel autoclave and reacted at 150 °C for 6 h. The results demonstrated that the yield of benzaldehyde reached 18%, and H<sub>2</sub> signals were again detected. Hence, we considered that the cleavage of meso-hydrobenzoin involves direct dehydrogenation and the breaking of C–C bonds.

To gain more insight into the reaction mechanism, the cleavage of the meso-hydrobenzoin process was studied by DFT calculations. Figure 7 illustrates the energy changes of catalytic meso-hydrobenzoin cleavage on Fe@NC-800 surface and its direct breaking of C–C bonds without catalysis. Moreover, the optimized structures as well as the transition state (TS) structures are shown in Figure 7. Apparently, the energy barrier of meso-hydrobenzoin molecule to TS is up to 5.53 eV without catalysis. However, on the surface of the Fe@NC-800 nanosphere catalyst, this part of the energy barrier requires only 2.75 eV, which is almost half of the former. It can be inferred that the energy barrier for the cleavage of meso-hydrobenzoin is significantly decreased on the surface of the Fe@NC-800 nanosphere catalyst, providing a plausible explanation for its superior catalytic performance.

**3.4. Adaptability of the Fe@NC-800 Nanosphere Catalyst.** This catalytic system was applied to other vicinal diol substrates with the optimized reaction conditions (Table 3). First, (R,R) or (S,S)-hydrobenzoin (Table 3, 1b, 1c) were cleaved to benzaldehyde (Table 3, 2a) with yields of 92 and 96%, respectively (Table 3, entries 1–2). Subsequently, symmetrical and asymmetrical benzylic diols (Table 3, 1e–1f) were successfully converted into the corresponding product (Table 3, 5a) with a satisfactory yield upon extending the reaction time and raising the temperature (Table 3, entries 3–5). The substrates (Table 3, 1g–1i) gave the target product (Table 3, 2b–2e) in excellent yields. Furthermore, the presence of electron-donating group did not affect the reactions (Table 3, entries 6–8). The substrates (Table 3, 1j–1k) were converted to the corresponding products (Table 3, 2e–2f) with the yields of 99 and 93%, respectively (Table 3, entries 9,10). The structures of some target products and non-commercially available disubstituted vicinal diols were determined by <sup>1</sup>H and <sup>13</sup>C NMR spectra (see Figures S4–S9).

Furthermore, tandem reactions were developed for the synthesis of N-containing products with high added-value by utilizing H<sub>2</sub> generated during the cleavage of meso-hydrobenzoin, and the product structures were determined by GC–MS spectrogram (Figure S10). First, the tandem reaction between meso-hydrobenzoin and aniline was used as a model

Table 3. Cleavage of Internal 1,2-Diols<sup>a</sup>

Entry	Substrates	Products	Time (h)	Yield (%)
1			6	92
2			6	96
3 <sup>b</sup>			12	95
4 <sup>b</sup>			12	99
5 <sup>b</sup>			12	93
6			6	99
7			6	98
8			6	99
9			6	99
10 <sup>b</sup>			6	93

<sup>a</sup>Reaction conditions: substrates (0.25 mmol), toluene (5 mL), Fe@NC-800 (0.27 mol %), 110 °C, N<sub>2</sub> (0.4 MPa). <sup>b</sup>130 °C.

reaction to screen the optimal reaction conditions. Several pivotal parameters, such as reaction temperature, reaction time, and catalyst dosage, were explored in detail (Table S5). Notably, the Fe@NC-800 catalyst exhibited the highest catalytic performance at 160 °C after a 24 h reaction period with a catalyst dosage of 0.41 mol %, reaching a 94% yield of *N*-benzylaniline (7a). Accordingly, the tandem reaction mechanism, as elucidated by characterization findings and corroborated by DFT analysis, entails two principal processes: C–C bond cleavage is an autologous hydrogen transfer event. In detail, the vicinal diol undergoes cleavage of C–C bonds on the surface of the Fe@NC-800 catalyst, resulting in the formation of benzaldehyde and hydrogen. Subsequently, benzaldehyde reacts swiftly with aniline to generate an imine intermediate through a condensation reaction. Finally, this imine intermediate is promptly reduced by the hydrogen generated from the process of C–C bond cleavage, leading to the generation of the high value-added *N*-benzylaniline product.

Next, a series of tandem reaction sequences were carried out with meso-hydrobenzoin and aniline derivatives. As illustrated in Figure 8, a range of aniline derivatives with electron-deficient and electron-rich of aromatic substituents partici-



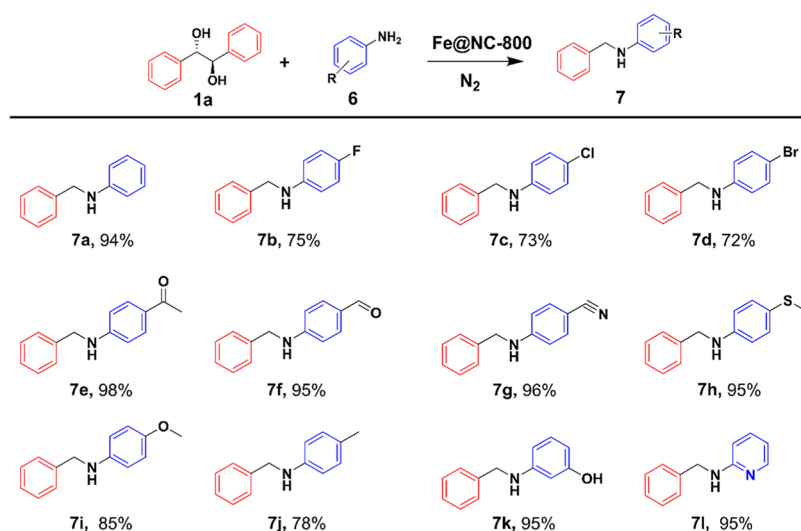


**Figure 8.** Catalytic activity of Fe@NC-800 in the tandem reaction between meso-hydrobenzoin and aniline derivatives. Reaction conditions: 1a (0.35 mmol), 6 (0.25 mmol), Fe@NC-800 (0.41 mol %), toluene (5 mL), N<sub>2</sub> (0.4 MPa), 160 °C, 24 h.

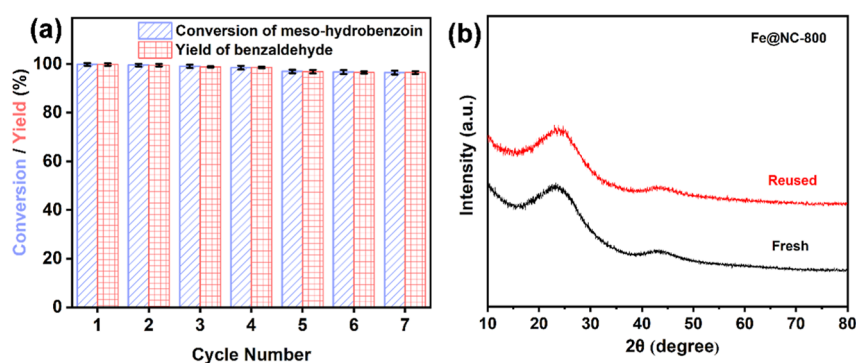


**Figure 9.** (a) Reusability test of Fe@NC-800 catalyst. (Reaction conditions: 0.25 mmol substrates, 5 mL of toluene, 0.27 mol % catalyst, 110 °C, 0.4 MPa of N<sub>2</sub>), (b) XRD patterns of fresh and reused Fe@NC-800 in this work.

pated in corresponding multistep, one-pot reaction with meso-hydrobenzoin, and most processes afforded the target amine products (Figure 8, 7a-7n) with excellent yields. Specifically, *N*-benzylaniline (Figure 8, 7a) was obtained in a 94% yield. The electron-deficient monosubstituted aniline derivatives gave the corresponding products (Figure 8, 7b-7d) in moderate yields. The reactions were not affected by the presence of carbonyl, aldehyde or cyano substituent on the benzene ring of aniline derivatives. High yields of 98 and 96% were achieved for the respective amine products (Figure 8, 7e, 7g). In addition, the electron-rich monosubstituted aniline derivatives also successfully produced the target second amine products (Figure 8, 7h-7k) with excellent yield. Furthermore, 2-aminopyridine was converted to the corresponding product (Figure 8, 7l) with 95% yield. These results reveal that the Fe@NC-800 nanosphere catalyst is highly applicable for the conversion of vicinal diols to high value-added N-containing compounds. Various routes have been reported for the conventional synthesis of benzylaniline, including benzylation reaction, cross-coupling reaction and amination with aldehydes or ketones etc.<sup>52–54</sup> However, the above approach also suffers from the disadvantages of the use of toxic and corrosive reagents or reducing agents, lower product selectivity, nonrecyclability, and a limited range of substrates. In contrast, the Fe@NC-800 nanosphere catalytic system generates secondary amines in high efficiency and selectivity without

any additives, offering a new pathway for acquiring high value-added secondary amine products. Nevertheless, the methodology is not without its limitations, such as the complexity of the synthetic procedure and the challenges related to scaling up to industrial production levels. These issues need to be addressed in future research.

**3.5. Reusability Test of the Fe@NC-800 Nanosphere Catalyst.** To evaluate the reusability of the catalyst, the Fe@NC-800 nanosphere catalyst was employed in the cleavage of meso-hydrobenzoin. Figure 9a illustrated that the conversion of meso-hydrobenzoin and the yield of benzaldehyde exhibited a decrease of no more than 2% after 7 successive cycles. The Fe content in both the initial reaction solution of the fresh catalysts and the reaction solution after seven cycles was analyzed by using ICP to determine the potential leaching of Fe species (Table S6). The results demonstrated that the leached Fe content in the first and seventh reacted solutions was negligible, which indicated that the good recyclability of the catalyst. The stability of Fe@NC-800 was tested by DTA/TGA analysis. As shown in Figure S12, weight losses of about 16 and 18% from 30 to 1000 °C were observed in the TGA/DTA curves of the fresh Fe@NC-800 and reused Fe@NC-800 catalysts, respectively. Within the temperature range of 30 to 160 °C, the weight loss of fresh Fe@NC-800 and reused Fe@NC-800 catalysts was approximately 2.2 and 3.6%, respectively. Thus, the Fe@NC-800 catalyst shows good stability within our



catalytic system. In addition, the structural integrity of the reused Fe@NC-800 nanosphere catalyst was verified through various characterization including XRD patterns, TEM, SEM and N<sub>2</sub> adsorption–desorption isotherms (Figures 9b and S11). The results confirmed that the crystal structure and morphology of the Fe@NC-800 nanosphere catalyst remained basically unchanged after repeated use. The specific surface area decreased slightly. The collected data support the conclusion that the Fe@NC-800 nanosphere catalyst demonstrates remarkable stability and reusability, positioning it as a potential candidate for environmentally friendly chemical processing.

## 4. CONCLUSIONS

In conclusion, three ultralow loading Fe supported on N-doped carbon nanosphere catalysts were prepared and applied in the high value-added transformation of vicinal diols through C–C bonds cleavage and autologous hydrogen transfer strategy under N<sub>2</sub> atmosphere. The catalyst was prepared using a hard template method with acid etching, leading to high dispersion of Fe species in the Fe@NC-800 nanosphere catalyst, as confirmed by characterization results. The highly dispersed Fe species was confirmed as the active sites through a poisoning experiment. Control experiments and DFT calculations confirmed that the outstanding performance was due to the highly dispersed Fe species at the active sites. Besides, a series of high value-added N-containing products could be generated from meso-hydrobenzoin and corresponding aniline derivatives, indicating the wide adaptability of the Fe@NC-800 nanosphere catalyst. Furthermore, the catalytic behavior of the Fe@NC-800 nanosphere catalyst for the reusability test had no significant decrease, showing its good reusability. This work offers new avenues for the facile synthesis of high value-added N-containing compounds from sustainable vicinal diols.

## ■ ASSOCIATED CONTENT

### SI Supporting Information

The Supporting Information is available free of charge at <https://pubs.acs.org/doi/10.1021/acsanm.4c03304>.

Detailed synthesis information on noncommercial vicinal diol and corresponding NMR data, SEM, and TEM images, XPS spectra, GC–MS spectrogram, and N<sub>2</sub> adsorption–desorption isotherms (PDF)

## ■ AUTHOR INFORMATION

### Corresponding Authors

**Yan Zhou** – National Engineering Research Center for Carbohydrate Synthesis, Key Laboratory of Fluorine and Silicon for Energy Materials and Chemistry of Ministry of Education, School of Chemical Engineering, Jiangxi Normal University, Nanchang 330022, China; [orcid.org/0000-0003-0108-5061](https://orcid.org/0000-0003-0108-5061); Email: [anitachow@jxnu.edu.cn](mailto:anitachow@jxnu.edu.cn)

**Wei Hui** – National Engineering Research Center for Carbohydrate Synthesis, Key Laboratory of Fluorine and Silicon for Energy Materials and Chemistry of Ministry of Education, School of Chemical Engineering, Jiangxi Normal University, Nanchang 330022, China; School of Life Science, Jingtangshan University, Ji'an 343009, China; [orcid.org/0000-0002-3228-6037](https://orcid.org/0000-0002-3228-6037); Email: [whui@jgsu.edu.cn](mailto:whui@jgsu.edu.cn)

## Authors

**Fei-Feng Mao** – National Engineering Research Center for Carbohydrate Synthesis, Key Laboratory of Fluorine and Silicon for Energy Materials and Chemistry of Ministry of Education, School of Chemical Engineering, Jiangxi Normal University, Nanchang 330022, China

**Yi-An Wang** – School of Life Science, Jingtangshan University, Ji'an 343009, China; [orcid.org/0000-0003-2133-5363](https://orcid.org/0000-0003-2133-5363)

**Ming-Shuai Sun** – National Engineering Research Center for Carbohydrate Synthesis, Key Laboratory of Fluorine and Silicon for Energy Materials and Chemistry of Ministry of Education, School of Chemical Engineering, Jiangxi Normal University, Nanchang 330022, China; [orcid.org/0000-0002-5126-4159](https://orcid.org/0000-0002-5126-4159)

**Duan-Jian Tao** – National Engineering Research Center for Carbohydrate Synthesis, Key Laboratory of Fluorine and Silicon for Energy Materials and Chemistry of Ministry of Education, School of Chemical Engineering, Jiangxi Normal University, Nanchang 330022, China; [orcid.org/0000-0002-8835-0341](https://orcid.org/0000-0002-8835-0341)

Complete contact information is available at: <https://pubs.acs.org/doi/10.1021/acsanm.4c03304>

## Notes

The authors declare no competing financial interest.

## ■ ACKNOWLEDGMENTS

We thank the National Natural Science Foundation of China (22378178); the Key Lab of Fluorine and Silicon for Energy Materials and Chemistry of Ministry of Education, Jiangxi Normal University (KFSEMC-202209).

## ■ REFERENCES

- (1) Deng, W.; Feng, Y.; Fu, J.; Guo, H.; Guo, Y.; Han, B.; Jiang, Z.; Kong, L.; Li, C.; Liu, H.; Nguyen, P. T. T.; Ren, P.; Wang, F.; Wang, S.; Wang, Y.; Wang, Y.; Wong, S. S.; Yan, K.; Yan, N.; Yang, X.; Zhang, Y.; Zhang, Z.; Zeng, X.; Zhou, H. Catalytic Conversion of Lignocellulosic Biomass into Chemicals and Fuels. *Green Energy Environ.* **2023**, *8* (1), 10–114.
- (2) Liao, Y.; de Beeck, B. O.; Thielemans, K.; Ennaert, T.; Snelders, J.; Dusselier, M.; Courtin, C. M.; Sels, B. F. The Role of Pretreatment in the Catalytic Valorization of Cellulose. *Mol. Catal.* **2020**, *487*, 110883.
- (3) Chen, Z.; Wan, C. Biological Valorization Strategies for Converting Lignin into Fuels and Chemicals. *Renewable Sustainable Energy Rev.* **2017**, *73*, 610–621.
- (4) Weng, C.; Peng, X.; Han, Y. Depolymerization and Conversion of Lignin to Value-Added Bioproducts by Microbial and Enzymatic Catalysis. *Biotechnol. Biofuels* **2021**, *14* (1), 84.
- (5) Carpentier, R.; Denis, W.; Sanz Azcona, F.; Carraro, D.; Grauwels, G.; Orlandi, M.; Zonta, C.; Licini, G.; Bartik, K. Vanadium Catalyst in Micelles: Toward a Greener Aerobic Oxidative Cleavage of Vicinal Diols in Water. *ACS Sustain. Chem. Eng.* **2023**, *11* (23), 8633–8641.
- (6) Guicheret, B.; Da Silva, E.; Philippe, R.; Favre-Reguillon, A.; Vanoye, L.; Blach, P.; Raoul, Y.; De Bellefon, C.; Métaf, E.; Lemaire, M. Aerobic Oxidative Cleavage of Vicinal Diol Fatty Esters by a Supported Ruthenium Hydroxide Catalyst. *ACS Sustain. Chem. Eng.* **2020**, *8* (35), 13167–13175.
- (7) Guo, P.; Liao, S.; Wang, S.; Shi, J.; Tong, X. Highly Efficient and Selectivity-Controllable Aerobic Oxidative Cleavage of C–C Bond over Heterogeneous Fe-Based Catalysts. *J. Catal.* **2021**, *395*, 399–403.
- (8) Amadio, E.; González-Fabra, J.; Carraro, D.; Denis, W.; Gjoka, B.; Zonta, C.; Bartik, K.; Cavani, F.; Solmi, S.; Bo, C.; Licini, G.

Efficient Vanadium-Catalyzed Aerobic C-C Bond Oxidative Cleavage of Vicinal Diols. *Adv. Synth. Catal.* **2018**, *360* (17), 3286–3296.

(9) Escande, V.; Lam, C. H.; Grison, C.; Anastas, P. T. Ecomnox, a Biosourced Catalyst for Selective Aerobic Oxidative Cleavage of Activated 1,2-Diols. *ACS Sustain. Chem. Eng.* **2017**, *5* (4), 3214–3222.

(10) Zhou, Z. z.; Liu, M.; Lv, L.; Li, C. J. Silver(I)-Catalyzed Widely Applicable Aerobic 1,2-Diol Oxidative Cleavage. *Angew. Chem., Int. Ed.* **2018**, *57* (10), 2616–2620.

(11) Escande, V.; Lam, C. H.; Coish, P.; Anastas, P. T. Heterogeneous Sodium-Manganese Oxide Catalyzed Aerobic Oxidative Cleavage of 1,2-Diols. *Angew. Chem., Int. Ed.* **2017**, *56* (32), 9561–9565.

(12) Luo, H.; Wang, L.; Shang, S.; Niu, J.; Gao, S. Aerobic Oxidative Cleavage of 1,2-Diols Catalyzed by Atomic-Scale Cobalt-Based Heterogeneous Catalyst. *Commun. Chem.* **2019**, *2* (1), 17.

(13) Kim, S. M.; Kim, D. W.; Yang, J. W. Transition-Metal-Free and Chemoselective Naotbu-O<sub>2</sub>-Mediated Oxidative Cleavage Reactions of Vic-1,2-Diols to Carboxylic Acids and Mechanistic Insight into the Reaction Pathways. *Org. Lett.* **2014**, *16* (11), 2876–2879.

(14) Weber, M. A.; Ford, P. C. Catalytic Dehydrogenation of 1,2- and 1,3-Diols. *J. Mol. Catal. A: Chem.* **2016**, *416*, 81–87.

(15) Sato, H.; Tamura, M.; Nakagawa, Y.; Tomishige, K. Synthesis of  $\alpha$ -Hydroxy Ketones from Vicinal Diols by Selective Dehydrogenation over Ir-Reox/SiO<sub>2</sub> Catalyst. *Chem. Lett.* **2014**, *43* (3), 334–336.

(16) Li, M.; Zhang, C.; Tang, Y.; Chen, Q.; Li, W.; Han, Z.; Chen, S.; Lv, C.; Yan, Y.; Zhang, Y.; Zheng, W.; Wang, P.; Guo, X.; Ding, W. Environment Molecules Boost the Chemoselective Hydrogenation of Nitroarenes on Cobalt Single-Atom Catalysts. *ACS Catal.* **2022**, *12* (19), 11960–11973.

(17) Yang, W.; Liu, X.; Chen, X.; Cao, Y.; Cui, S.; Jiao, L.; Wu, C.; Chen, C.; Fu, D.; Gates, I. D.; Gao, Z.; Jiang, H. L. A Sulfur-Tolerant MOF-Based Single-Atom Fe Catalyst for Efficient Oxidation of No and Hg<sub>0</sub>. *Adv. Mater.* **2022**, *34* (20), 2110123.

(18) Wang, C.; Han, Y.; Tian, M.; Li, L.; Lin, J.; Wang, X.; Zhang, T. Main-Group Catalysts with Atomically Dispersed in Sites for Highly Efficient Oxidative Dehydrogenation. *J. Am. Chem. Soc.* **2022**, *144* (37), 16855–16865.

(19) Liu, H.; Li, X.; Ma, Z.; Sun, M.; Li, M.; Zhang, Z.; Zhang, L.; Tang, Z.; Yao, Y.; Huang, B.; Guo, S. Atomically Dispersed Cu Catalyst for Efficient Chemoselective Hydrogenation Reaction. *Nano Lett.* **2021**, *21* (24), 10284–10291.

(20) Zhou, P.; Jiang, L.; Wang, F.; Deng, K.; Lv, K.; Zhang, Z. High Performance of a Cobalt-Nitrogen Complex for the Reduction and Reductive Coupling of Nitro Compounds into Amines and Their Derivatives. *Sci. Adv.* **2017**, *3*, No. e1601945.

(21) Han, S.; Sun, M.-S.; Chen, W.-T.; Zhou, Y.; Tao, D.-J. Highly Active Co<sub>1</sub>-N<sub>3</sub>-O<sub>1</sub> Single-Atom Catalyst for Boosting Catalytic Synthesis of Unsaturated Benzylamines and Arylamines. *Chem. Eng. J.* **2024**, *480*, 148330.

(22) Wei, X.; Hu, Z.; Li, C.; Zhang, Y.; Xie, X.; Wang, H.; Wu, Z. High-Density Atomically Dispersed CoNx Catalysts Supported on Nitrogen-Doped Mesoporous Carbon Materials for Efficient Hydrogenation of Nitro Compounds. *Catal. Today* **2022**, *405–406*, 92–100.

(23) Ghaedi, H.; Zhao, M. Review on Template Removal Techniques for Synthesis of Mesoporous Silica Materials. *Energy Fuels* **2022**, *36* (5), 2424–2446.

(24) Kumar, P.; Matoh, L.; Srivastava, V. C.; Štangar, U. L. Synthesis of Zinc/Ferrocyanide Nano-Composite Catalysts Having a High Activity for Transesterification Reaction. *Renewable Energy* **2020**, *148*, 946–952.

(25) Erdogan, B.; Arbag, H.; Yasyerli, N. SBA-15 Supported Mesoporous Ni and Co Catalysts with High Coke Resistance for Dry Reforming of Methane. *Int. J. Hydrogen Energy* **2018**, *43* (3), 1396–1405.

(26) Li, Y.; Jiang, C.; Chen, X.; Jiang, Y.; Yao, C. Yb<sup>3+</sup>-Doped Two-Dimensional Upconverting Tb-Mof Nanosheets with Luminescence Sensing Properties. *ACS Appl. Mater. Interfaces* **2022**, *14* (6), 8343–8352.

(27) Mallakpour, S.; Abdolmaleki, A.; Tabesh, F. Ultrasonic-Assisted Manufacturing of New Hydrogel Nanocomposite Biosorbent Containing Calcium Carbonate Nanoparticles and Tragacanth Gum for Removal of Heavy Metal. *Ultrason. Sonochem.* **2018**, *41*, 572–581.

(28) Li, W.; Li, J.; Hu, C.; Xiao, Q. Research on Pore-Fracture Characteristics and Adsorption Performance of Main Coal Seams in Lvjiatuo Coal Mine. *Processes* **2023**, *11* (6), 1700.

(29) Tang, Y.; Fung, V.; Zhang, X.; Li, Y.; Nguyen, L.; Sakata, T.; Higashi, K.; Jiang, D.-e.; Tao, F. F. Single-Atom High-Temperature Catalysis on a Rh<sub>1</sub>O<sub>3</sub> Cluster for Production of Syngas from Methane. *J. Am. Chem. Soc.* **2021**, *143* (40), 16566–16579.

(30) Miao, W.; Liu, Y.; Wang, D.; Du, N.; Ye, Z.; Hou, Y.; Mao, S.; Ostrikov, K. The Role of Fe-Nx Single-Atom Catalytic Sites in Peroxymonosulfate Activation: Formation of Surface-Activated Complex and Non-Radical Pathways. *Chem. Eng. J.* **2021**, *423*, 130250.

(31) Chirani, M. R.; Kowsari, E.; SalarAmoli, H.; Yousefzadeh, M.; Chinnappan, A.; Ramakrishna, S. Covalently Functionalized Graphene Oxide with Cobalt-Nitrogen-Enriched Complex Containing Iodide Ligand as Charge Carrier Nanofiller for Eco-Friendly High Performance Ionic Liquid-Based Dye-Sensitized Solar Cell. *J. Mol. Liq.* **2021**, *325*, 115198.

(32) Bokhonov, B. B.; Dudina, D. V.; Sharafutdinov, M. R. Graphitization of Synthetic Diamond Crystals: A Morphological Study. *Diamond Relat. Mater.* **2021**, *118*, 108563.

(33) Noh, S. C.; Lee, S. Y.; Shul, Y. G.; Jung, K.-D. Sulfuric Acid Decomposition on the Pt/N-Sic Catalyst for Si Cycle to Produce Hydrogen. *Int. J. Hydrogen Energy* **2014**, *39* (9), 4181–4188.

(34) Khan, H. A.; Natarajan, P.; Jung, K.-D. Stabilization of Pt at the Inner Wall of Hollow Spherical SiO<sub>2</sub> Generated from Pt/Hollow Spherical Sic for Sulfuric Acid Decomposition. *Appl. Catal., B* **2018**, *231*, 151–160.

(35) Yang, L.; Zhen, S. J.; Li, Y. F.; Huang, C. Z. Silver Nanoparticles Deposited on Graphene Oxide for Ultrasensitive Surface-Enhanced Raman Scattering Immunoassay of Cancer Biomarker. *Nanoscale* **2018**, *10* (25), 11942–11947.

(36) González-García, P.; Arenas-Esteban, D.; Ávila-Brandé, D.; Urones-Garrote, E.; Otero-Díaz, L. Nickelocene as Precursor of Microporous Organometallic-Derived Carbon and Nickel Oxide-Carbon Nanocomposite. *J. Colloid Interface Sci.* **2017**, *490*, 410–419.

(37) Chang, P.; Mei, H.; Zhao, Y.; Pan, L.; Zhang, M.; Wang, X.; Cheng, L.; Zhang, L. Nature-Inspired 3d Spiral Grass Structured Graphene Quantum Dots/Mxene Nanohybrids with Exceptional Photothermal-Driven Pseudo-Capacitance Improvement. *Adv. Sci.* **2022**, *9* (30), 2204086.

(38) Lazauskas, A.; Marcinauskas, L.; Andrulevicius, M. Modification of Graphene Oxide/V<sub>2</sub>O<sub>5</sub>·nH<sub>2</sub>O Nanocomposite Films Via Direct Laser Irradiation. *ACS Appl. Mater. Interfaces* **2020**, *12* (16), 18877–18884.

(39) Han, J.; Meng, X.; Lu, L.; Bian, J.; Li, Z.; Sun, C. Single-Atom Fe-N<sub>x</sub>-C as an Efficient Electrocatalyst for Zinc–Air Batteries. *Adv. Funct. Mater.* **2019**, *29* (41), 1808872.

(40) Du, N.; Liu, Y.; Li, Q.; Miao, W.; Wang, D.; Mao, S. Peroxydisulfate Activation by Atomically-Dispersed Fe-Nx on N-Doped Carbon: Mechanism of Singlet Oxygen Evolution for Nonradical Degradation of Aqueous Contaminants. *Chem. Eng. J.* **2021**, *413*, 127545.

(41) Xia, D.; Yang, X.; Xie, L.; Wei, Y.; Jiang, W.; Dou, M.; Li, X.; Li, J.; Gan, L.; Kang, F. Direct Growth of Carbon Nanotubes Doped with Single Atomic Fe-N4 Active Sites and Neighboring Graphitic Nitrogen for Efficient and Stable Oxygen Reduction Electrocatalysis. *Adv. Funct. Mater.* **2019**, *29* (49), 1906174.

(42) Yi, S.; Qin, X.; Liang, C.; Li, J.; Rajagopalan, R.; Zhang, Z.; Song, J.; Tang, Y.; Cheng, F.; Wang, H.; Shao, M. Insights into KMnO<sub>4</sub> Etched N-Rich Carbon Nanotubes as Advanced Electrocatalysts for Zn-Air Batteries. *Appl. Catal., B* **2020**, *264*, 118537.

(43) Zhang, N.; Zhou, T.; Chen, M.; Feng, H.; Yuan, R.; Zhong, C. a.; Yan, W.; Tian, Y.; Wu, X.; Chu, W.; Wu, C.; Xie, Y. High-Purity

Pyrrole-Type FeN<sub>4</sub> Sites as a Superior Oxygen Reduction Electrocatalyst. *Energy Environ. Sci.* **2020**, *13* (1), 111–118.

(44) Chen, Y.; Li, Z.; Zhu, Y.; Sun, D.; Liu, X.; Xu, L.; Tang, Y. Atomic Fe Dispersed on N-Doped Carbon Hollow Nanospheres for High-Efficiency Electrocatalytic Oxygen Reduction. *Adv. Mater.* **2018**, *31* (8), 1806312.

(45) Gao, W.; Tang, S.; Wu, T.; Wu, J.; Cheng, K.; Xia, M. Solid Fe Resources Separated from Rolling Oil Sludge for Co Oxidation. *Int. J. Mol. Sci.* **2022**, *23* (20), 12134.

(46) Zhang, L.; Li, C.; Liu, Y.; Xu, C.; Zhang, Y. Unraveling Active Sites Regulation and Temperature-Dependent Thermodynamic Mechanism in Photothermocatalytic CO<sub>2</sub> Conversion with H<sub>2</sub>O. *npj Comput. Mater.* **2024**, *10* (1), 132.

(47) Zhang, L.; Wang, B.; Hu, J.; Huang, X.; Ma, W.; Li, N.; Wågberg, T.; Hu, G. Nickel-Induced Charge Redistribution in Ni-Fe/Fe<sub>3</sub>C@Nitrogen-Doped Carbon Nanocage as a Robust Mott-Schottky Bi-Functional Oxygen Catalyst for Rechargeable Zn-Air Battery. *J. Colloid Interface Sci.* **2022**, *625*, 521–531.

(48) Balasamy, R. J.; Tope, B. B.; Khurshid, A.; Al-Ali, A. A. S.; Atanda, L. A.; Sagata, K.; Asamoto, M.; Yahiro, H.; Nomura, K.; Sano, T.; Takehira, K.; Al-Khattaf, S. S. Ethylbenzene Dehydrogenation over FeOx/(Mg,Zn)(Al)O Catalysts Derived from Hydrotalcites: Role of MgO as Basic Sites. *Appl. Catal., A* **2011**, *398* (1–2), 113–122.

(49) Zhang, J.; Shi, K.; An, Z.; Zhu, Y.; Shu, X.; Song, H.; Xiang, X.; He, J. Acid-Base Promoted Dehydrogenation Coupling of Ethanol on Supported Ag Particles. *Ind. Eng. Chem. Res.* **2020**, *59* (8), 3342–3350.

(50) Quesada, J.; Faba, L.; Díaz, E.; Ordóñez, S. Copper-Basic Sites Synergic Effect on the Ethanol Dehydrogenation and Condensation Reactions. *ChemCatChem* **2018**, *10* (16), 3583–3592.

(51) Abdulrazzaq, H. T.; Rahmani Chokanlu, A.; Frederick, B. G.; Schwartz, T. J. Reaction Kinetics Analysis of Ethanol Dehydrogenation Catalyzed by MgO-SiO<sub>2</sub>. *ACS Catal.* **2020**, *10* (11), 6318–6331.

(52) Heravi, M. M.; Kheilkordi, Z.; Zadsirjan, V.; Heydari, M.; Malmir, M. Buchwald-Hartwig Reaction: An Overview. *J. Organomet. Chem.* **2018**, *861*, 17–104.

(53) Mäki-Arvela, P.; Simakova, I. L.; Murzin, D. Y. One-Pot Amination of Aldehydes and Ketones over Heterogeneous Catalysts for Production of Secondary Amines. *Catal. Rev.* **2023**, *65* (2), 501–568.

(54) Mahmudov, I.; Demir, Y.; Sert, Y.; Abdullayev, Y.; Sujayev, A.; Alwasel, S. H.; Gulcin, I. Synthesis and Inhibition Profiles of N-Benzyl- and N-Allyl Aniline Derivatives against Carbonic Anhydrase and Acetylcholinesterase - a Molecular Docking Study. *Arabian J. Chem.* **2022**, *15* (3), 103645.